J. Fluid Mech. (2005), *vol.* 542, *pp.* 53–67. © 2005 Cambridge University Press
doi:10.1017/S0022112005006129 Printed in the United Kingdom

Steady zonal flows in spherical shell dynamos

By JULIEN AUBERT
Max-Planck-Institute for Solar System Research, Max-Planck-Strasse 2,
37191 Katlenburg-Lindau, Germany
jaubert@gwdg.de

(Received 22 July 2004 and in revised form 11 May 2005)

Convective dynamos in a rotating spherical shell feature steady zonal flows. This process is studied numerically for Prandtl numbers of 0.1 and 1, Ekman numbers in the range $E = 10^{-4}$–10^{-5}, magnetic Prandtl number from 0.5 to 10 and Rayleigh numbers up to 100 times supercritical. The zonal flow is mainly of thermal wind origin, and minimizes the shear of the axisymmetric poloidal magnetic field lines, according to Ferraro's law of corotation. The dissipation in the interior of the fluid is mainly ohmic, while the introduction of rigid velocity boundary conditions confines viscous dissipation in the Ekman boundary layers. The root-mean-square amplitude U_φ of the zonal flow in the spherical shell scales as $U_\varphi = (F/\Omega)^{0.5}$, F being the buoyancy flux through the shell and Ω the rotation rate. As a consequence of the corotation law, this scaling relationship is remarkably independent of the magnetic field amplitude. It does not depend on thermal, kinematic and magnetic diffusivities, owing to the large-scale and steady nature of forcing and dissipative processes. The scaling law is in agreement with the zonal-flow amplitude at the external boundary of the Earth's liquid core.

1. Introduction

Steady azimuthal flows are common in the fluids of planetary systems and stars. They can be observed, for instance, in the atmosphere, the oceans, in the liquid iron core of the Earth, as well as on the surface, and possibly the interior of large fluid planets like Jupiter and Saturn. A fluid initially at rest in a rotating frame (in solid-body rotation in a Galilean frame) and subject to thermal convection can gain mean angular momentum in two ways. The first mode is purely axisymmetric: baroclinic flows can couple with the Coriolis force to create a zonal thermal wind. This occurs where iso-density lines cross iso-gravity lines, i.e where density varies in the lateral direction, in thin or thick spherical shells (see for instance Aurnou *et al.* 2003). As identified by Busse (1970), the second mode involves nonlinear effects: small-scale, turbulent convective eddies can excite the zonal flow if the associated Reynolds stresses have a non-vanishing axisymmetric component. In thin shells such as the Earth's atmosphere, the effect of the Reynolds stresses can be understood through the inertial mixing of potential vorticity, which creates axisymmetric shear and therefore zonal flow (see Rhines & Young 1982; Hide & James 1983 and, more recently, the experiments of Aubert, Jung & Swinney 2002). To obtain a sizeable Reynolds stress effect in thick spherical shells, a high degree of correlation is required between the cylindrically radial and azimuthal velocity components of the small-scale eddies (Busse & Hood 1982; Christensen 2002). The dominant Coriolis force organizes the flow in columns parallel to the rotation axis (Proudman–Taylor constraint). Where the columns hit the sloping spherical boundaries, the non-penetration condition forces the two velocity components to correlate.

In rotating conducting fluids and plasmas, the convective motions can sustain a magnetic field. The Coriolis force is balanced by the Lorentz force (magnetostrophic balance), by a pressure gradient and, to a lesser extent, by buoyancy forces. Zonal flows interact strongly with magnetic fields: they are responsible for the omega dynamo effect which produces toroidal magnetic field from an initial poloidal field. This effect is essential for stellar alpha-omega dynamos, where differential rotation is strong. On the other hand, poloidal magnetic field lines carry magnetic tension and can oppose the development of an azimuthal flow in planetary alpha-squared dynamos such as the geodynamo, where differential rotation is weaker.

Numerous observations of the geomagnetic field suggest the existence of zonal flows in the Earth's liquid iron core (see for instance Pais & Hulot 2000; Finlay & Jackson 2003). The complexity of the relations that tie zonal flows to magnetic fields motivates the present study. I use numerical models of self-sustained convective dynamos to analyse the time-averaged zonal flow, in comparison with non-magnetic convection. In that respect, the present paper is an extension of the numerical study of Christensen (2002) to cases where dynamo action is present. The use of rigid boundary conditions also provides a numerical test to experimental results acquired by Aubert *et al.* (2001) and Aurnou *et al.* (2003). For non-magnetic convection, the nonlinear Reynolds stresses are the preferred forcing mode for zonal flow. In the presence of a dynamo, the Proudman–Taylor constraint is relaxed by the magnetic forces, the highly columnar organization of the flow is destroyed and the thermal wind forcing of zonal flow becomes dominant.

2. Equations and numerical method

2.1. *General formulation*

A spherical coordinate system (r, θ, φ) with unit vectors $(\boldsymbol{e}_r, \boldsymbol{e}_\theta, \boldsymbol{e}_\varphi)$ is chosen. The magnetohydrodynamic equations for the velocity $\boldsymbol{u}$, magnetic induction $\boldsymbol{B}$ and temperature T are solved for a conducting and convecting Boussinesq fluid within a spherical shell, rotating about the $\boldsymbol{e}_z$-axis of rotation. In the dimensionless form chosen by Christensen (2002) they are

$$\frac{\partial \boldsymbol{u}}{\partial t} + \boldsymbol{u}\cdot\nabla\boldsymbol{u} + 2\boldsymbol{e}_z \times \boldsymbol{u} + \nabla P = Ra^* \, \frac{\boldsymbol{r}}{r_o} T + \frac{E}{P_m}(\nabla \times \boldsymbol{B}) \times \boldsymbol{B} + E\nabla^2 \boldsymbol{u}, \tag{2.1}$$

$$\frac{\partial \boldsymbol{B}}{\partial t} = \nabla \times (\boldsymbol{u} \times \boldsymbol{B}) + \frac{E}{Pm}\nabla^2 \boldsymbol{B}, \tag{2.2}$$

$$\frac{\partial T}{\partial t} + \boldsymbol{u}\cdot\nabla T = \frac{E}{Pr}\nabla^2 T, \tag{2.3}$$

$$\nabla\cdot\boldsymbol{u} = 0, \tag{2.4}$$

$$\nabla\cdot\boldsymbol{B} = 0. \tag{2.5}$$

The inverse of the rotation rate Ω^{-1} is chosen as the time scale. The length scale is the shell thickness D. The magnetic induction is scaled by $(\rho\mu\lambda\Omega)^{1/2}$, where ρ is the fluid density, λ is the magnetic diffusivity, and μ the magnetic permeability of the fluid. The temperature is scaled by the difference ΔT between the inner and the outer boundary. The radial coordinate is denoted by r, r_i and r_o are respectively the inner and outer radii of the shell. The four dimensionless parameters are the modified Rayleigh number Ra^*, the Ekman number E, the Prandtl number Pr and the magnetic Prandtl number Pm:

$$Ra^* = \frac{\alpha g_o \Delta T}{\Omega^2 D}, \tag{2.6}$$

$$E = \frac{\nu}{\Omega D^2}, \tag{2.7}$$

$$Pr = \frac{\nu}{\kappa}, \tag{2.8}$$

$$Pm = \frac{\nu}{\lambda}. \tag{2.9}$$

Here α is the thermal expansion coefficient, g_o the gravity at the outer boundary, ν is the kinematic viscosity, and κ is the thermal diffusivity of the fluid. The modified Rayleigh number Ra^* is used and can be related to the traditional Rayleigh number $Ra = \alpha g_o \Delta T D^3/\kappa\nu$ by:

$$Ra^* = Ra\ E^2\ Pr^{-1}. \tag{2.10}$$

The main advantage of choosing Ω^{-1} as the time scale is to introduce the modified Rayleigh number Ra^*. Unlike the traditional Rayleigh number, Ra^* does not depend on the fluid diffusivities ν and κ. It is the natural parameter to express scaling laws in a regime where these diffusivities do not play a major role.

The heat-flux based Rayleigh number will also be used in this study:

$$Ra_q^* = Nu^* Ra^* = \frac{r_o}{r_i} \frac{\alpha g_o q}{\rho C_p \Omega^3 D^2}, \tag{2.11}$$

where q is the convective heat flux per unit surface at the outer boundary and C_p is the specific heat.

$$Nu^* = \frac{r_o}{r_i} \frac{q}{\rho C_p \Delta T \Omega D} \tag{2.12}$$

is a modified Nusselt number, which can be related to the traditional Nusselt number $Nu = (r_o/r_i) q D/\rho C_p \kappa \Delta T D$ by:

$$Nu^* = Nu\ E\ Pr^{-1}. \tag{2.13}$$

The vector fields $\boldsymbol{u}$ and $\boldsymbol{B}$ are decomposed into poloidal and toroidal potentials. These potentials and the temperature T are expanded into spherical harmonics in the lateral direction, with maximum degree and order l_{max}, and into Chebyshev polynomials in the radial direction, up to degree $N_r - 2$ where N_r is the number of radial grid points. An azimuthal symmetry parameter m_s is introduced: the computation time can be reduced by solving only for modes or order $m = 0$, $m_s, 2m_s, 3m_s, \ldots$.

The velocity field $\boldsymbol{u}$ satisfies rigid boundary conditions. The inner core is freely rotating under the influence of magnetic and viscous torques, and has the same conductivity as the outer core. The outer boundary is insulating. In most calculations, the temperature difference between the boundaries is fixed. Some calculations have a fixed heat flux at the outer boundary, while the temperature at the inner boundary is fixed. In the former case, Ra_q^* is not really an input parameter, since it requires knowledge of the Nusselt number which is an output of the calculation. In the latter case, Ra_q^* is entirely an input parameter.

The numerical implementation MAGIC by Wicht (2002) is used.

2.2. *Equations for the zonal flow*

Let the square brackets [ ] be the azimuthal averaging operator, and the angle brackets $\langle\ \rangle$ be the time averaging operator. The derivative of the zonal flow velocity $u_\varphi = [\boldsymbol{u}]_\varphi = [\boldsymbol{u}]\cdot\boldsymbol{e_\varphi}$ along the axis of rotation is given by the classical thermal wind balance, obtained by retaining the three largest terms (buoyancy, Lorentz force and Coriolis force the viscous and inertial terms being presumably lower by a factor E) in $[\nabla\times(2.1)]_\varphi$:

$$\frac{1}{E}\frac{\partial u_\varphi}{\partial z} = \frac{Ra^*}{2Er_o}\frac{\partial[T]}{\partial\theta} - \frac{1}{2Pm}(\nabla\times[(\nabla\times\boldsymbol{B})\times\boldsymbol{B}])_\varphi. \tag{2.14}$$

Once $\partial u_\varphi/\partial z$ is known, The description of u_φ can be completed by the knowledge of its value at the outer boundary. Applying the operator [ ] to (2.1) and projecting onto the azimuthal unit vector $\boldsymbol{e_\varphi}$ yields:

$$\frac{\partial u_\varphi}{\partial t} + [(\boldsymbol{u}\cdot\nabla)\boldsymbol{u}]_\varphi + 2[\boldsymbol{u}]_s = E[\nabla^2\boldsymbol{u}]_\varphi + \frac{E}{Pm}[(\nabla\times\boldsymbol{B})\times\boldsymbol{B}]_\varphi, \tag{2.15}$$

where the s coordinate is the cylindrical radius. The equation governing the column-averaged zonal flow can be obtained by integrating (2.15) in the $\boldsymbol{e_z}$-direction of the rotation axis:

$$\frac{\partial}{\partial t}\int_L u_\varphi \mathrm{d}z + \underbrace{\int_L [(\boldsymbol{u}\cdot\nabla)\boldsymbol{u}]\,\mathrm{d}z}_{I_R} + \underbrace{2\int_L [u]_s\,\mathrm{d}z}_{I_C} = \underbrace{\int_L E[\nabla^2\boldsymbol{u}]_\varphi\,\mathrm{d}z}_{I_V} + \underbrace{\int_L \frac{E}{Pm}[(\nabla\times\boldsymbol{B})\times\boldsymbol{B}]_\varphi\,\mathrm{d}z}_{I_L}, \tag{2.16}$$

where L is a fluid column parallel to $\boldsymbol{e_z}$, excluding the viscous layer at the external spherical boundary. Applying the time averaging operator yields:

$$\langle I_C\rangle = \langle I_L\rangle + \langle I_V\rangle - \langle I_R\rangle. \tag{2.17}$$

If the outer viscous boundary layer behaves as an Ekman layer, then the integral $\langle I_C\rangle$ can be related to the zonal velocity close to the outer boundary (Greenspan 1968), outside the tangent cylinder:

$$\langle I_C\rangle = \frac{2E^{1/2}}{\sqrt{|\cos\theta|}}\langle u_N\rangle, \tag{2.18}$$

where $\langle u_N\rangle$ is the steady zonal flow observed at both ends of fluid column L (all the calculations presented in this study have equator-symmetric steady zonal flows). The validity of (2.18) will be checked in detail in the results section. Equations (2.17) and (2.18) directly relate the steady core surface flow $\langle u_N\rangle$ to the integrals of Lorentz force, divergence of the Reynolds stresses and viscous forces within the fluid shell. Together with the time average of (2.14), they allow for a complete description of the time-averaged zonal flow in the shell.

A power budget for the zonal flow will be used to clarify the sources and sinks of energy. Multiplying (2.15) by u_φ yields:

$$\frac{1}{2}\frac{\partial u_\varphi^2}{\partial t} = \underbrace{-[(\boldsymbol{u}\cdot\nabla)\boldsymbol{u}]_\varphi\cdot u_\varphi}_{P_R} \underbrace{-2[\boldsymbol{u}]_s\cdot u_\varphi}_{P_C} + \underbrace{\frac{E}{Pm}[(\nabla\times\boldsymbol{B})\times\boldsymbol{B}]_\varphi\cdot u_\varphi}_{P_L} + \underbrace{E[\nabla^2\boldsymbol{u}]_\varphi\cdot u_\varphi}_{P_V} \tag{2.19}$$

Here P_R is the power transferred to zonal flow through the divergence of the Reynolds stresses, and P_C is the power exchanged between zonal and meridional flows by the

Coriolis force. Since the Coriolis force does no work, but exchanges work between components of the flow, $-P_C$ appears in a power budget written for the meridional flow. The remaining power terms P_L and P_V are, respectively, the power transferred to the zonal flow by the Lorentz and viscous forces.

2.3. *Set of numerical models*

The radius ratio is fixed to $r_i/r_o = 0.35$. The control parameters Ra^*, E, Pm and Pr are variable and 43 numerical simulations of rotating convection and convective dynamo are analysed. The temperature boundary conditions are of type ΔT (both boundaries at fixed temperature) or Φ (the inner boundary has fixed temperature, the heat flux is fixed at the outer boundary). Although no particular symmetry has been assumed, the time-averaged zonal velocity field is always found to be symmetric with respect to the equator.

A model is dipole-dominated if more than half of the magnetic energy is in the magnetic dipole. The parameters and results for all simulations are summarized in table 1. Some cases draw particular attention: case D is the basic dipole-dominated dynamo case, case C is the corresponding convection case. Case D′ ($m_s = 1$) is used together with case D ($m_s = 2$) to verify that assuming $m_s \neq 1$ has little impact on the solution. Cases D1 to D5 explore the effect of a varying magnetic Prandtl number. Case DR is not dipole-dominated, in contrast with case D which is.

The critical Rayleigh number Ra_c is determined by time-stepping the linear part of the simulation and determining the growth rate of each mode.

The state of the system is diagnosed using the zonal kinetic energy E_φ, as well as the magnetic energy E_m:

$$E_\varphi = \frac{1}{2V_s}\int_{V_s} u_\varphi^2 \,\mathrm{d}V, \tag{2.20}$$

$$E_m = \frac{E}{2P_m V_s}\int_{V_s} \boldsymbol{B}^2 \,\mathrm{d}V, \tag{2.21}$$

where V_s is the volume of the spherical shell. The root-mean square time-averaged zonal flow U_φ and Elsasser number Λ are defined as

$$U_\varphi = \sqrt{2\langle E_\varphi\rangle}, \tag{2.22}$$

$$\Lambda = \frac{2P_m}{E}\langle E_m\rangle. \tag{2.23}$$

3. Results

3.1. *Zonal flows in convection and dynamo models*

Figure 1 compares the time-averaged zonal flow of cases C (non-magnetic convection) and D (self-sustained dynamo). Cases C and D have been selected for analysis because they are numerically the least costly cases presenting a typical behaviour. The large-scale zonal flow structure of cases C and D is indeed robust against variation of E when the thermal forcing is large enough (Ra a few times critical). The large-scale zonal flow structure of case D, as well as the flow amplitude (see constant U_φ in cases D, D2, D3, D4 and D5) are almost independent of the magnetic Prandtl number once the Lorentz force has reached sufficient strength to equilibrate the Coriolis force, i.e. once $\Lambda > 1$. The zonal flow structure is robust against variations of Ra until

Case	Ra/Ra_c	P_m	Nu	Λ	U_φ	l_{max}	N_r	m_s	dipole-dominated
			$E = 10^{-4}$,	$Pr = 1$,	$(Ra_c = 6.95 \times 10^5)$,	ΔT			
	1.29	0	1.06	0	1.3×10^{-4}	64	33	1	
	1.44	0	1.08	0	2.03×10^{-4}	64	33	1	
	2.88	0	1.27	0	1.07×10^{-3}	64	41	1	
	4.32	0	1.49	0	2.11×10^{-3}	64	41	1	
	4.32	2	1.63	0.74	8.23×10^{-4}	64	41	1	Y
	7.20	0	2.20	0	2.62×10^{-3}	64	41	1	
	7.20	2	2.38	4.21	1.62×10^{-3}	64	41	1	Y
C	10.8	0	3.03	0	3.91×10^{-3}	84	41	2	
D2	10.8	0.5	3.33	0.67	2.3×10^{-3}	84	41	2	Y
D3	10.8	1	3.29	2.4	2.25×10^{-3}	84	41	2	Y
D	10.8	2	3.33	6.70	2.17×10^{-3}	84	41	2	Y
D′	10.8	2	3.37	6.62	2.25×10^{-3}	84	41	1	Y
D4	10.8	6	3.51	28.3	2.25×10^{-4}	84	41	2	Y
D5	10.8	10	3.51	63	2.3×10^{-4}	84	41	2	Y
	21.6	0	5.96	0	1.2×10^{-2}	128	65	4	
	21.6	2	5.47	7.62	5.3×10^{-3}	128	65	4	Y
	43.2	0	9.01	0	2.6×10^{-2}	128	65	4	
	43.2	2	8.15	9.72	1.0×10^{-2}	128	65	4	N
	86.4	2	11.03	20.3	1.67×10^{-2}	170	65	4	N
			$E = 10^{-4}$,	$Pr = 0.1$,	$(Ra_c = 2.85 \times 10^5)$,	ΔT			
	10.9	2	2.1	60	1.08×10^{-2}	84	41	2	Y
DR	26.3	2	3.5	51	4.01×10^{-2}	128	65	4	N
	52.6	2	5.0	110	5.55×10^{-2}	128	65	4	N
	105	2	6.4	189	9.75×10^{-2}	128	65	4	N
			$E = 10^{-5}$,	$Pr = 1$,	$(Ra_c = 1.06 \times 10^7)$,	ΔT			
	1.42	0	1.08	0	2.7×10^{-5}	64	41	1	
	2.83	0	1.24	0	1.58×10^{-4}	64	41	1	
	4.72	0	1.77	0	3.2×10^{-4}	64	41	1	
	4.72	2	1.72	0.56	1.65×10^{-4}	64	41	1	Y
	7.08	0	1.92	0	3.9×10^{-4}	128	65	4	
	7.08	2	2.38	2.42	2.94×10^{-4}	128	65	4	Y
	9.43	0	2.5	0	5.6×10^{-4}	128	65	4	
	9.43	2	3.54	6.36	4.07×10^{-4}	128	65	4	Y
	14.2	0	3.61	0	9.8×10^{-4}	170	65	4	
	14.2	2	5.13	15.2	5.84×10^{-4}	170	65	4	Y
	18.9	0	5.5	0	1.68×10^{-3}	170	65	4	
	18.9	2	6.5	18.5	8.5×10^{-4}	170	81	4	Y
	37.7	0	12.4	0	6.62×10^{-3}	256	97	8	
	37.7	2	11.	27.7	1.6×10^{-3}	212	81	4	Y
	Ra_Q/Ra_{Qc}		$E = 10^{-4}$,	$Pr = 1$,	$(Ra_{Qc} = 6.95 \times 10^5)$,	Φ			
	10.8	2		2.09	1.8×10^{-3}	84	41	2	Y
	21.6	2		8.64	2.8×10^{-3}	84	41	2	Y
	43.2	2		10.28	3.6×10^{-3}	84	41	2	Y
	86.4	2		11.44	4.7×10^{-3}	84	41	2	Y
	172.8	2		7.52	7.3×10^{-3}	128	65	4	N
	345.6	2		8.48	1.4×10^{-3}	128	65	4	N

TABLE 1. Numerical simulations and results for $r_i/r_o = 0.35$. Temperature boundary conditions are: ΔT for fixed temperature at both boundaries, Φ for fixed temperature at inner boundary and fixed heat flux at outer boundary.

the regime identified by Kutzner & Christensen (2002) where the magnetic dipole collapses.

The columnar structure of the zonal flow in case C (figure 1*a*) is a consequence of the geostrophic equilibrium between the Coriolis and pressure forces in (2.1). Taking the curl of (2.1) indeed yields the Proudman–Taylor constraint $\partial \boldsymbol{u}/\partial z \approx 0$ when the two forces dominate the others. The zonal flow takes its energy from the non-axisymmetric scales of the flow through the divergence $[(\boldsymbol{u}\cdot\nabla)\boldsymbol{u}]_\varphi$ of the nonlinear Reynolds stresses in (2.15) (Busse 1970; Busse & Hood 1982; Aubert *et al.* 2001; Christensen 2002). A columnar flow usually increases the efficiency of the energy transfer between non-axisymmetric and axisymmetric scales.

Figures 1(*b*) and 1(*c*) show that in case D the structure of u_φ is very different. The geostrophic, z-independent part does not dominate. Indeed the Elsasser number is of order 1, which means that the Lorentz force equilibrates the Coriolis force in amplitude and the Proudman–Taylor constraint on geostrophy is relaxed.

The magnetic field and the zonal flow co-exist under a principle of minimal interaction known as Ferraro's law of corotation (Ferraro 1937): the time-averaged axisymmetric magnetic field lines follow the iso-contours of the time-averaged u_φ/s, where s is the cylindrical radius. Where this is not the case, an axisymmetric azimuthal magnetic field is created from the axisymmetric meridional field at a rate $p_\omega = s\nabla(u_\varphi/s)\cdot\boldsymbol{B}$ due to the omega effect. The production of azimuthal magnetic field increases the magnetic tension along the meridional field lines, and is proportional to $\boldsymbol{B}^2$. In agreement with the Lenz law, the resulting Lorentz force tends to oppose the forces that increased the magnetic tension, i.e. reduce p_ω and therefore align contours of u_φ/s with magnetic field lines. The white lines on figures 1(*b*) and 1(*c*) represent this restoring action (contours of $(1/Pm)\nabla\times[(\nabla\times\boldsymbol{B})\times\boldsymbol{B})]_\varphi$), and correlate indeed with places where zonal flow contours cross the magnetic field lines. In a time snapshot (figure 1(*b*), the restoring action is typically much stronger than in the time average (figure 1*c*), where the minimal interaction is found.

Since the dynamo zonal flow is not geostrophic, it makes sense to look at the thermal wind balance (2.14). The residues on figure 2 show that this balance is verified in the time average, as well as at any moment in time, i.e. that the viscous and inertial terms neglected in (2.14) are negligible here. For a time average, as already seen in figure 1, the restoring contribution of the Lorentz force $(1/Pm)\nabla\times[(\nabla\times\boldsymbol{B})\times\boldsymbol{B})]_\varphi$ is much smaller than in any snapshot, and is negligible when compared to the other terms in (2.14). The magnetic tension indeed grows with a decreasing radius of a magnetic loop. The time-averaged structure of the magnetic field is large-scale, and along these large magnetic loops the magnetic tension is weak. A stronger tension is carried by smaller loops on figure 2(*a*), but these loops vanish in the time average.

The magnetic field has therefore no direct influence on the variations of the zonal flow along $\boldsymbol{e}_z$. It does however influence the parameter Ra_q^* since the relaxation of the Proudman–Taylor constraint allows an enhanced transport of heat. Figure 3 shows that the isothermal lines of case D stack up near the boundaries, while the Nusselt numbers reported in table 1 are higher for dynamos.

In figure 4, the time-averaged zonal flow of a non dipole-dominated model (case DR) is now compared to case D. Outside the tangent cylinder the zonal flow in case DR is closer to the non-magnetic case C. Inside the tangent cylinder, the thermal wind structure is more pronounced in case DR than in in case C. The alignment of magnetic lines with zonal flow contours is broken.

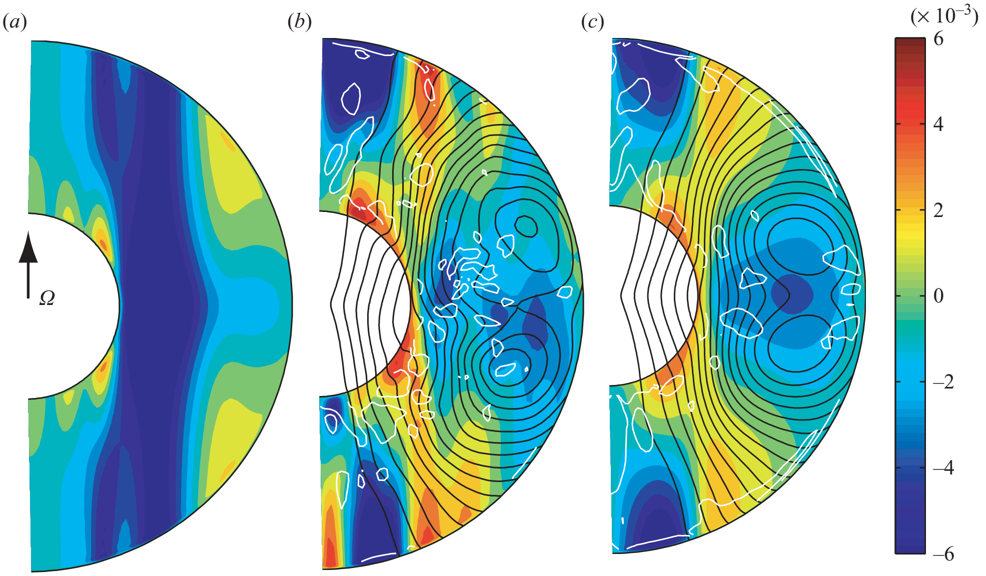

FIGURE 1. Meridional sections (*a*) of the time-averaged zonal flow in the convection case C (blue is westwards, red eastwards); (*b*). a snapshot in time of the zonal flow in dynamo case D, with, in black, superimposed lines of the axisymmetric meridional magnetic field. In white, isolines −100 and 100 of $(1/Pm)\nabla \times [(\nabla \times \boldsymbol{B}) \times \boldsymbol{B})]_{\varphi}$; (*c*) the time-averaged zonal flow in case D, same conventions as (*b*), isolines −20 and 20 of $(1/Pm)\nabla \times [(\nabla \times \boldsymbol{B}) \times \boldsymbol{B}]_{\varphi}$.

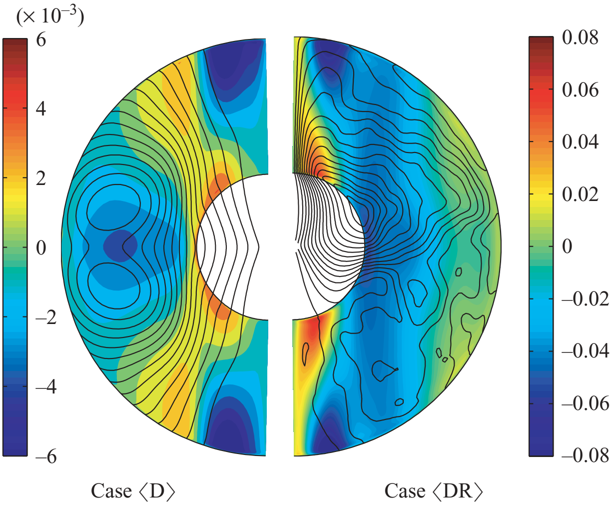

FIGURE 4. Meridional sections of the time-averaged zonal flow (blue is westwards) and axisymmetric poloidal magnetic field lines for cases D and DR.

3.2. *Power budget*

The presence of the magnetic field dramatically changes the structure of the zonal flow, but does not seem to power it directly. To clarify this point, the time-average of the power budget (2.19) is analysed in figure 5.

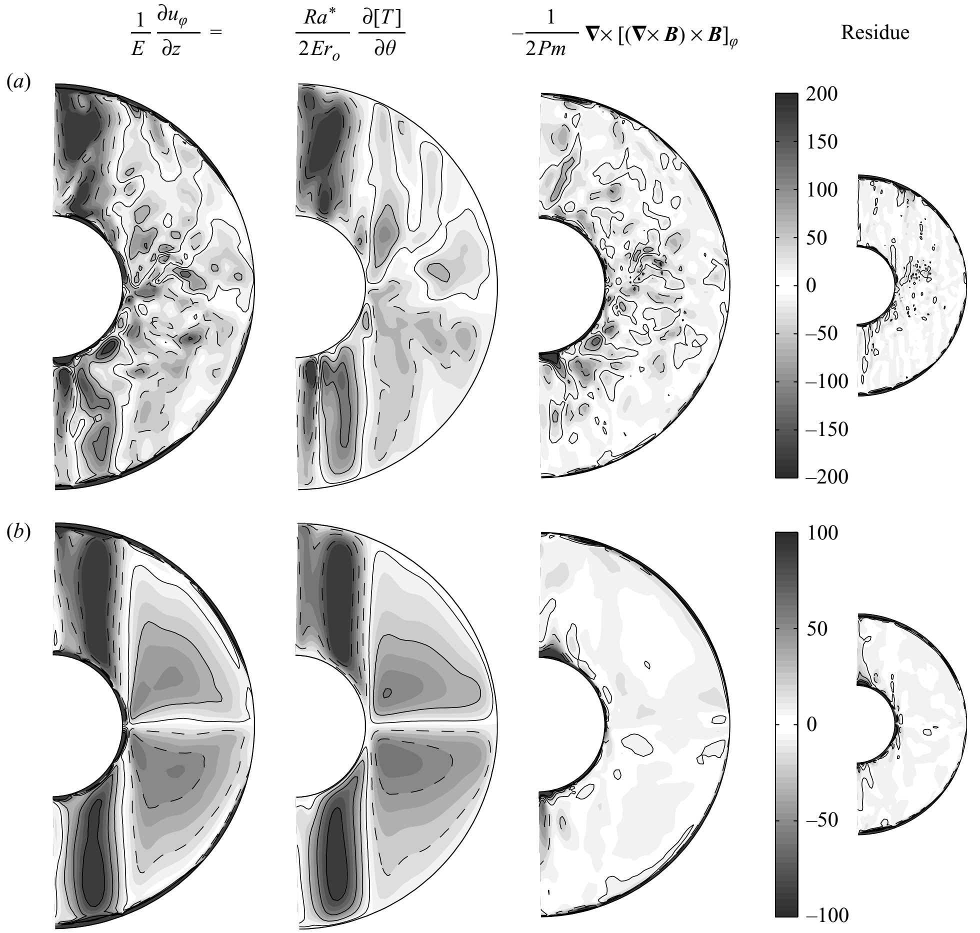

FIGURE 2. The thermal wind balance (2.14) for case D in (*a*) a snapshot in time, and (*b*) the time-average. Plain contours: positive values; dashed contours: negative values.

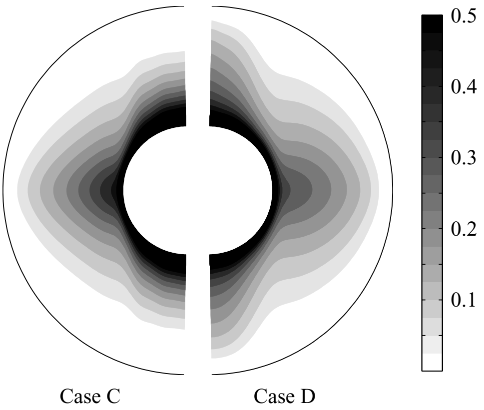

FIGURE 3. Meridional cuts of $\langle [T] \rangle$. The magnetic fields allows for an enhanced heat flux through the relaxation of the Proudman–Taylor constraint.

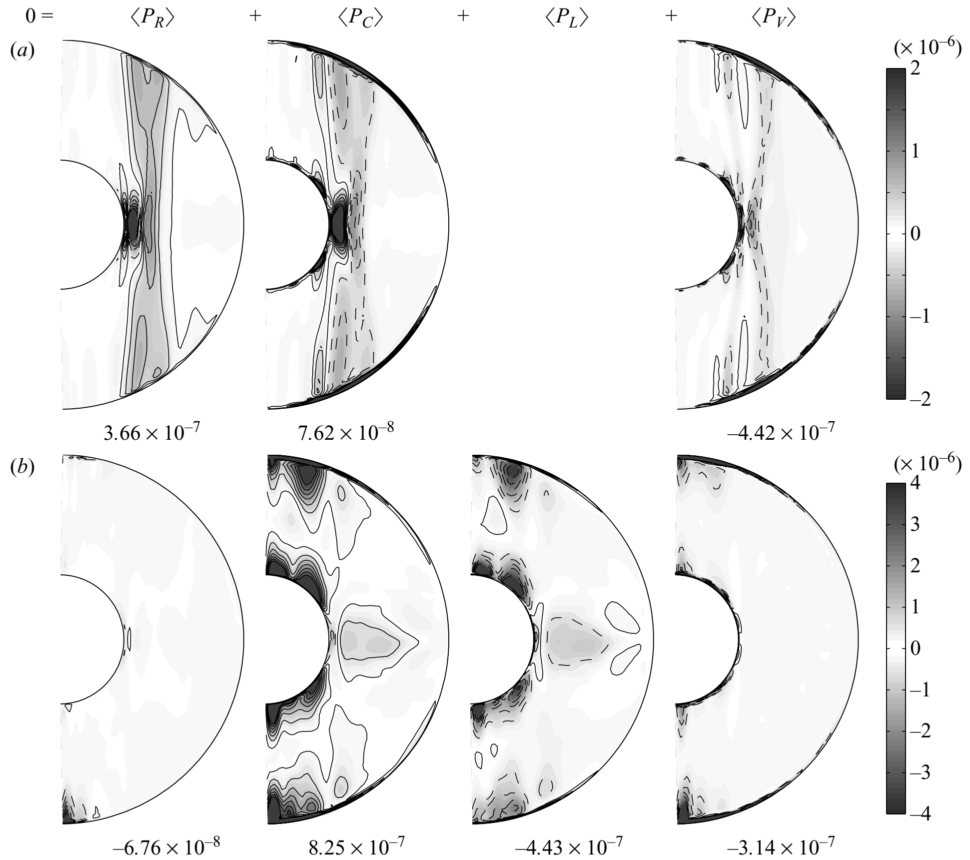

FIGURE 5. Time-averaged power budget of cases (*a*) C and (*b*) D (plain contours: power sources; dashed contours: power sinks). The shell integral of the time-averaged power is reported below each diagram.

In case C, the flow is driven mainly by the divergence of the Reynolds stresses. This forcing mode is efficient because of the columnar structure of the non-axisymmetric flow. The shell integral of $\langle P_R \rangle$ is almost entirely balanced by $\langle P_V \rangle$. The power is therefore dissipated through Ekman friction in the viscous boundary layers.

In case D, the power source is now $\langle P_C \rangle$, with strong contributions where lateral buoyancy variations are important. A baroclinic meridional flow is first created, which couples with the Coriolis force to create a thermal wind zonal flow. The power dissipation is equally distributed between Ohmic dissipation in the interior of the fluid ($\langle P_L \rangle$) and viscous dissipation in the Ekman boundary layers ($\langle P_V \rangle$). The Reynolds stresses are not significant in this case. From an energetic point of view, the Lorentz force therefore enters the dynamics of the zonal flow only as a dissipative mechanism.

In figure 6, the time-averaged power budget of case DR is analysed. In this case the forcing is almost equally distributed between the Reynolds stresses and the thermal wind. This is compatible with the shape observed in figure 4, where geostrophic flow and thermal wind are mixed. Dissipation is still equally distributed between the Lorentz force in the interior and the viscous friction in the Ekman boundary layers.

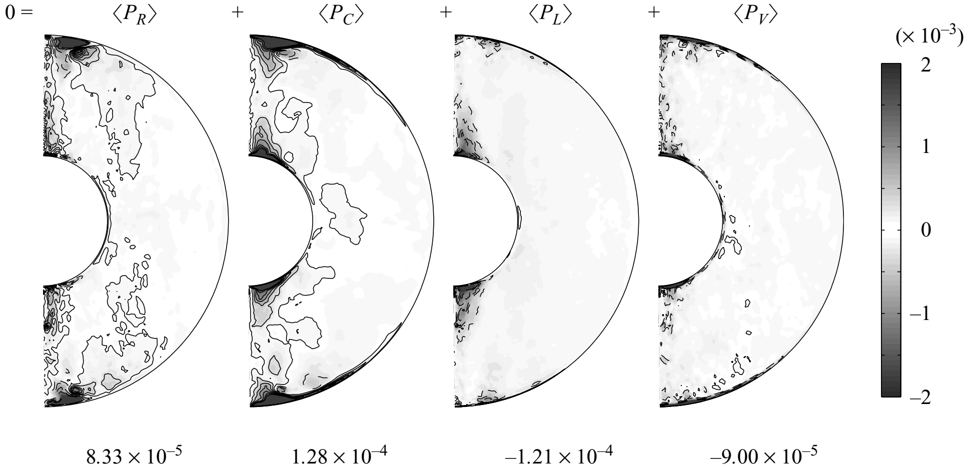

FIGURE 6. Time-averaged power budget of case DR, same conventions as figure 5.

3.3. *Value of the zonal flow at the outer boundary*

The time-average of (2.15) is analysed in figure 7(*a*). In the interior of the fluid the axisymmetric φ components of the Coriolis and Lorentz forces (first and second sections in figure 7*a*) dominate the inertial and viscous effects. The column-integrated terms of (2.17) are represented in figure 7(*b*). The upper panel is a check for formula (2.18). It shows that this formula holds outside the tangent cylinder, but also inside the tangent cylinder. This is due to the co-rotation of the inner core, which minimizes the viscous boundary-layer effects at the inner boundary. The fact that (2.18) holds shows that magnetic effects are negligible on the Ekman layers.

The lower panel highlights the dominant role of $\langle I_L \rangle$ for balancing $\langle I_C \rangle$, the Ekman friction of the surface zonal flow. However, I_L is not controlled by the local strength of the Lorentz force. This is a consequence of the partial enforcement of Taylor's constraint (see for instance Hollerbach 1996): there is some cancellation when the Lorentz force is integrated in the direction $\boldsymbol{e}_z$ to compute I_L. Indeed, figure 7 shows that $\langle I_L \rangle$ is roughly seven times smaller than the maximum value of the Lorentz force in the shell.

3.4. *Scaling of the zonal flow amplitude*

The magnetic field does not control directly the variations of the zonal flow in the direction of $\boldsymbol{e}_z$, neither does it control the value of the zonal flow at the outer boundary owing to the partial cancellation of the Lorentz force integral. Its main role is as a source of dissipation in the interior of the fluid. Therefore a scaling relation can be sought for the root-mean-square amplitude U_φ that does not depend on the magnetic field amplitude. The similarity between non-magnetic and magnetic thermal winds leads to consideration of the scaling proposed by Aurnou *et al.* (2003): using dimensional analysis, the local buoyancy available to drive the baroclinic flow can be estimated. Considering the thermal wind balance we then obtain:

$$U_\varphi = (Ra_q^*)^{0.5}. \tag{3.1}$$

Ra_q^* appears here as a measure of the available buoyancy. The numerical data set for dynamo cases in figure 8 supports an asymptote described well by (3.1) when the forcing is large. This proves the validity of the results acquired by Aurnou *et al.*

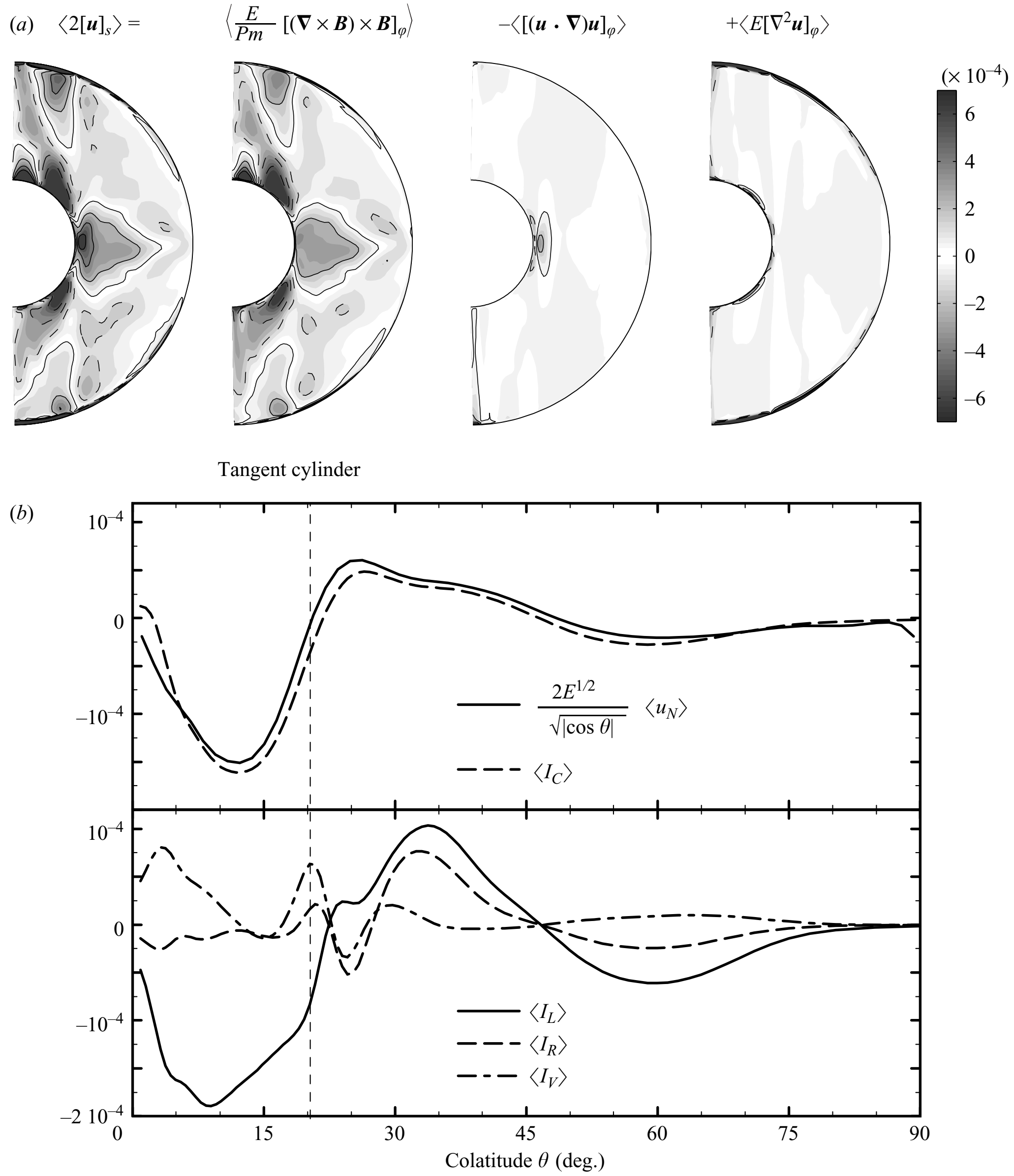

FIGURE 7. Case D. (*a*) Meridional cuts of the terms involved in the time average of (2.15). Plain contour lines are positive values, dashed contour lines are negative values. (*b*) Upper panel: test of the boundary-layer formula (2.18) showing its validity throughout the shell. Lower panel: z-integrals of the Lorentz, viscous forces and of the divergence of the Reynolds stresses.

(2003) when a self-sustained magnetic field is present. Note that the scaling applies irrespectively of the thermal boundary conditions used. The scaling also applies when high inertia and a non-dipole-dominated magnetic field are present such as in the models with $Pr = 0.1$.

Aubert *et al.* (2001) proposed a scaling for the amplitude U_φ of the zonal flow in their experiments of non-magnetic rotating convection. First, the non-axisymmetric

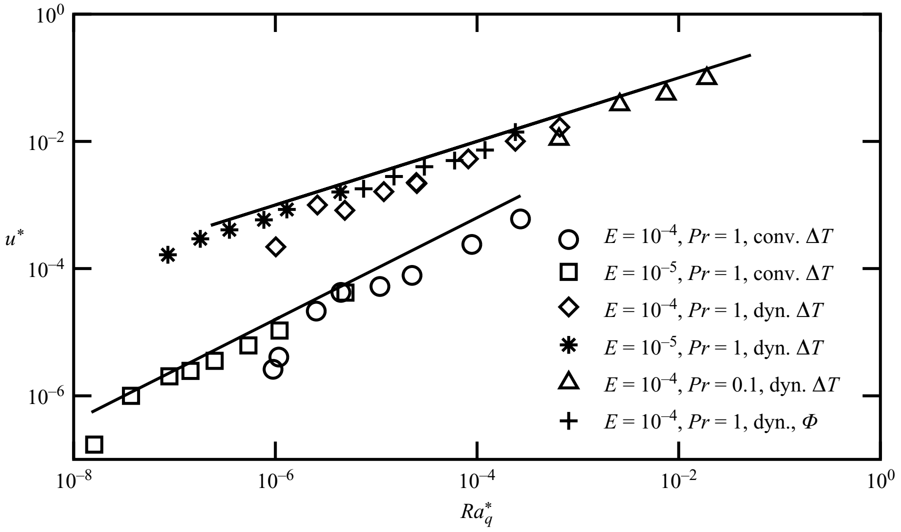

FIGURE 8. $u^* = E^{0.5}U_\varphi$ (convection) and $u^* = U_\varphi$ (dynamo) as a function of Ra_q^*. Upper black line: theoretical scaling (3.1). Lower black line: scaling (3.2).

convective flow is scaled as $(Ra_q^*)^{0.4}$ using an argument involving columnar flow and the conservation of potential vorticity. This scaling holds far from the convective onset. Then the amplitude of the divergence of the Reynolds stresses is supposed to scale as the squared convective flow, i.e. as $(Ra_q^*)^{0.8}$, owing to the good correlations between u_s and u_φ of the convective eddies. Finally, the Reynolds stresses are balanced by Ekman friction of the zonal flow on the outer boundary, which is exactly the mechanism identified in the power budget of the previous section. The resulting scaling relation is:

$$E^{0.5}U_\varphi = (Ra_q^*)^{0.8}. \tag{3.2}$$

This relation has been successfully tested against experimental data. The numerical values for non-magnetic convection in figure 8 approach an asymptote described well by (3.2) when the forcing is large, and this provides the first numerical confirmation of this scaling.

The difference in slope between asymptotes (3.2) and (3.1) is obvious in the numerical data set of figure 8. The behaviour of U_φ at large forcing reflects the change in the forcing and dissipation mechanisms, from convection to dynamo cases.

4. Discussion

In the models presented here, the thermal wind is forced at a large scale (the scale of the spherical shell), and the main part of the dissipation in the interior of the fluid is of ohmic nature, occurring at a large scale. The zonal flow is also time-averaged. Therefore the scaling relationship (3.1) does not depend on the diffusivities κ, ν and λ which, if they were present, would introduce a notion of scale and of dissipation rate in time. The simple form of (3.1) accounts for a simple geometry of zonal flow where small scales do not play a role in the time average.

The parameters of a real object such as the Earth's core are remote from those of the model. In particular, the magnetic Prandtl number is of order 10^{-6} and the Ekman number 10^{-14}, two values which are much lower than those used in the models. This raises questions as to the validity of the scaling relationship in the regime of the Earth. However, it has been noted that the underlying mechanism in (3.1) does not rely on any diffusive process in the system, and hence (3.1) does not depend on E, Pm and Pr. This suggests that the numerical computations in this study have reached an asymptotic regime where these processes do not play a role, and this allows for extrapolation to planetary objects. In dimensional form, the scaling relationship (3.1) writes $U_\varphi = (F/\Omega)^{0.5}$ where $F = \alpha g q/\rho C_p$ is the buoyancy flux through the spherical shell. The measured value of $U_\varphi = 10^{-4}\ \mathrm{m\,s^{-1}}$ for the polar vortex at the core–mantle boundary (Olson & Aurnou 1999) yields a buoyancy flux of $F = 10^{-12}\ \mathrm{m^2\,s^{-3}}$, a value which is in agreement with inner-core growth models of Aurnou *et al.* (2003).

It is generally believed that in the limit of vanishing Ekman number, the results of simulations with rigid and stress-free boundaries should converge. At a moderate Ekman number, the models presented in this study have several key differences with the dynamo calculations made by Grote & Busse (2001) with stress-free boundaries. In the computations of this study, the zonal flow has a low geostrophic part, is dominated by the thermal wind part and coexists with a dipole-dominated magnetic field. In the stress-free calculations of Grote & Busse (2001) the zonal flow has a dominant geostrophic part and coexists with a less, or non-dipole-dominated magnetic field. Indeed, with stress-free boundaries, the only limiting process for the geostrophic zonal flow is viscous friction in the interior of the fluid, which at high Ekman number allows for high values of this flow. Ferraro's law of corotation then makes the co-existence of a geostrophic zonal flow and a dominant dipole created by the dynamo difficult. This point is confirmed by the parameter-space study of dynamos with stress-free boundaries made by Busse & Simitev (2005). They found no dipolar dynamo at a Prandtl number of 0.1, where the geostrophic zonal flow dominates. At a Prandtl number of order one, dipolar dynamos can be found in a limited range of the convective forcing, where the geostrophic zonal flow competes with the thermal wind zonal flow. This range extends with decreasing Ekman number, suggesting a tendency of results acquired with rigid and stress-free boundaries to converge.

Dynamos with stress-free boundaries often exhibit magnetic fields having a strong asymmetry between the northern and the southern hemispheres, with an oscillatory time behaviour (Grote & Busse 2001), while the underlying flow components, and in particular the zonal flow, are as equator-symmetric as the flows shown in the present study. This can be understood using Ferraro's law of isorotation: a zonal flow shearing the axisymmetric poloidal magnetic field lines tends to create a field of the opposite polarity, thus leading to an oscillatory alpha–omega dynamo action. In the present study, the omega effect is small because the geostrophic zonal flow is weak, the dynamos have an alpha-squared mechanism and the oscillatory behaviour is not observed.

It is also interesting to compare stress-free and rigid boundaries in the case of non-magnetic convection (this study uses rigid boundaries whereas Christensen (2002) uses stress-free boundaries). At a moderate Ekman number, in both cases the geostrophic zonal flow is the dominant component, but this flow is stronger when stress-free boundaries are used. In the present rigid case indeed the zonal flow amplitude U_φ is limited by viscous friction in the Ekman boundary layers and scales like $U_\varphi = (Ra_q^*)^{0.8} E^{-0.5}$ (equation (3.2)). In the stress-free case, Christensen (2002) found $U_\varphi \propto (Ra_q^*)^{0.4}$, with no apparent dependence on the Ekman number but with a saturation level at high values of Ra_q^* due to a loss of correlation in the small scales of the convection flow. At lower Ekman numbers it is expected that the rigid case matches the stress-free case because a decreasing friction in the Ekman layer requires a stronger zonal flow.

Kutzner & Christensen (2002) have identified a regime boundary between dipole-dominated, and non-dipolar, reversing numerical dynamos. Ferraro's law of corotation prevents the coexistence of a strong columnar zonal flow and of a dominant magnetic dipole. Since the Reynolds stresses tend to force columnar zonal flows, it can be speculated that inertia plays a major role in the selection of a dominant dipole in the dynamo solution.

The author thanks J. Wicht, U. Christensen, J. Aurnou as well as three anonymous referees for comments and suggestions. Numerical calculations have been performed at the Gesellschaft für Wissenschaftliche Datenverarbeitung, Goettingen, Germany, and the Département de Modélisation Physique et Numérique, IPGP, Paris, France. This work has been supported by funding from the Max-Planck Society.

REFERENCES

Aubert, J., Brito, D., Nataf, H.-C., Cardin, P. & Masson, J. P. 2001 A systematic experimental study of spherical shell convection in water and liquid gallium. *Phys. Earth Planet. Int.* **128**, 51–74.

Aubert, J., Jung, S. & Swinney, H. 2002 Observations of zonal flow created by potential vorticity mixing in a rotating fluid. *Geophys. Res. Lett.* **29**(18), 1876, doi:10.1029/2002GL015422.

Aurnou, J., Andreadis, S., Zhu, L. & Olson, P. 2003 Experiments on convection in Earth's core tangent cylinder. *Earth Planet. Sci. Lett.* **212**, 119–134.

Busse, F. & Simitev, R. 2005 Prandtl-number dependence of convection-driven dynamos in rotating spherical fluid shells. *J. Fluid. Mech.* **532**, 365–388.

Busse, F. H. 1970 Differential rotation in stellar convection zones. *Astrophys. J.* **159**, 629–639.

Busse, F. H. & Hood, L. L. 1982 Differential rotation driven by a convection in a rapidly rotating annulus. *Geophys. Astrophys. Fluid Dyn.* **21**, 59–74.

Christensen, U. R. 2002 Zonal flow driven by strongly supercritical convection in rotating spherical shells. *J. Fluid. Mech.* **470**, 115–133.

Ferraro, V. C. A. 1937 The non-uniform rotation of the sun and its magnetic field. *Mon. Not. R. Astr. Soc.* **97**, 458.

Finlay, C. & Jackson, A. 2003 Equatorially dominated magnetic field change at the surface of Earth's core. *Science* **300**, 2084–2086.

Greenspan, H. P. 1968 *The Theory of Rotating Fluids*. Cambridge University Press.

Grote, E. & Busse, F. H. 2001 Dynamics of convection and dynamos in rotating spherical fluid shells. *Fluid. Dyn. Res.* **28**, 349–368.

Hide, R. & James, I. N. 1983 Differential rotation produced by potential vorticity mixing in a rapidly rotating fluid. *Geophys. J. R. Astr. Soc.* **74**, 301–312.

Hollerbach, R. 1996 On the theory of the geodynamo. *Phys. Earth Planet. Int.* **98**, 163–185.

Kutzner, C. & Christensen, U. 2002 From stable dipolar to reversing numerical dynamos. *Phys. Earth Planet. Int.* **131**, 29–45.

Olson, P. & Aurnou, J. 1999 A polar vortex in the Earth's core. *Nature* **402**, 170–173.

Pais, A. & Hulot, G. 2000 Length of day decade variations, torsional oscillations and inner core superrotation: evidence from recovered core surface zonal flows. *Phys. Earth Planet. Int.* **118**, 291–316.

Rhines, P. B. & Young, W. R. 1982 Homogenization of potential vorticity in planetary gyres. *J. Fluid. Mech.* **122**, 347–367.

Wicht, J. 2002 Inner-core conductivity in numerical dynamo simulations. *Phys. Earth Planet. Int.* **132**, 281–302.